Article

Enhancing Magnesium Phosphate Cement Paste for Efficient Fluoride Adsorption

Sana Gharsallah [1], Abdulrahman Alsawi [2,*], Abdulelah H. Alsulami [3], Clarence Charnay [4] and Mahmoud Chemingui [1]

[1] Laboratory of Inorganic Chemistry, LR17-ES-07, Faculty of Science, University of Sfax, Sfax 3018, Tunisia; sana.gharsallah.etud@fss.usf.tn (S.G.); mahmoud.chmingui@fss.usf.tn (M.C.)
[2] Department of Physics, College of Science, Qassim University, Buraidah 51452, Saudi Arabia
[3] Chemistry Department, Faculty of Science and Arts in Baljurashi, Al-Baha University, Al-Baha 65527, Saudi Arabia; aalsulami@bu.edu.sa
[4] Charles Gerhard Institut, UMR-5253 CNRS-UM-ENSCM, University of Montpellier, Place E, Bataillon, F-34095 Montpellier cedex 5, France; clarence.charnay@umontpellier.fr
* Correspondence: ansaoy@qu.edu.sa

Abstract: In the present study, we explore the synthesis and characterization of novel composite materials derived from magnesium phosphate cement by incorporating varying quantities of aluminum, iron oxide, or alumina. These composites demonstrate promising properties related to water resistance and significant specific surface areas. Furthermore, our investigations reveal that aluminum, iron oxide, and phosphate constituents exhibit an affinity for fluoride retention. Consequently, we apply these synthesized materials for fluoride adsorption. Our results indicate a noteworthy adsorption capacity, ranging from 2.35 mg/g for cement synthesized with 0.25 g of aluminum to 4.84 mg/g for materials synthesized with 1.5 g of aluminum. The influence of incorporating alumina or iron oxide into these matrices is thoroughly examined. Additionally, we investigated the optimal conditions utilizing a range of analytical techniques, including scanning electron microscopy (SEM) equipped with an energy dispersive spectrometer (EDS), the Brunauer–Emmett–Teller (BET) method, X-ray diffraction (XRD), Fourier-transform infrared spectroscopy (FTIR), and thermogravimetric analyses (TGA). To further elucidate this process, we perform equilibrium modeling and present experimental data in accordance with the Langmuir, Freundlich, Temkin, and Dubinin–Radushkevich isotherms.

Keywords: magnesium phosphate cement (MPC); X-ray diffraction; water purification; fluoride adsorption; isotherms; scanning electron microscopy

1. Introduction

Pollution presents an increasing threat to water, a basic resource that is essential to human survival. Pollution disturbs aquatic ecosystems and puts water safety at risk. Elevated amounts of harmful substances, either naturally occurring or due to human activity, are the cause of the contamination; the main contributors include agriculture, industrial operations, natural factors, and inadequate sewage treatment. In addition to affecting the health of aquatic ecosystems' fauna and flora, pollution also raises questions regarding the safety of water for human use and consumption [1,2].

Personalized and successful treatments are necessary to address these issues. Customized techniques are necessary due to the complexity of pollutants, which involves taking into account the many sources and types of contaminants found in water. Reducing water pollution requires strong sewage treatment facilities, stringent industrial discharge laws, and environmentally friendly farming methods. Furthermore, maintaining the long-term health of aquatic ecosystems and preserving the supply of safe water for the environment and human population depends heavily on public knowledge and active participation in water conservation initiatives [1–3]. Even at trace concentration levels in water, some

toxic elements can harm human health, which is why it is imperative to perform accurate studies on water quality. Commonly found in underground water are ions such as fluoride, nitrate, phosphate, and arsenic, which can be harmful to humans if ingested in excess. The third most common element in nature is fluoride, which is also one of the essential trace elements that, when consumed in the right amounts, has positive effects on the human skeletal system and teeth [4]. Fluoride, a prevalent natural contaminant, is found in the air, plants, and water. Nevertheless, to avert fluorosis, which predominantly impacts teeth and bones and leads to bone weakening by influencing the assimilation of calcium and phosphorus over an extended period, it is imperative to ensure that its concentration does not surpass 1.5 mg/L, according to the World Health Organization [2,4]. Additionally, elevated levels of fluoride can lead to liver damage, bone cancer, Alzheimer's syndrome, alterations in DNA structure, brain damage, and a reduction in children's IQ [5,6]. Effective treatment techniques include adsorption, reverse osmosis, membrane separation, ion exchange, and chemical treatment [5,6]. Among these, adsorption stands out for its flexibility, high efficiency, ease of operation, and cost-effectiveness compared to alternative techniques [7,8]. The utilization of adsorbent materials can often be economically viable, offering a practical solution for water treatment needs [9]. Commonly used adsorbents for fluoride removal include bone char, chitosan, activated carbon, zirconium–carbon hybrids, aluminum-based material, activated alumina, and other alternative and economical natural materials [7,10,11]. Moreover, materials that include rare earth elements are regarded as prospective adsorbents owing to their strong affinity for fluoride. Various metals, such as Y (III), Zr (IV), La (III), Ce (IV), Al (III), Cu (II), and Fe (III), are incorporated into carbonates, oxides, and hydroxides and play a significant role in capturing fluoride in water. Multiple research studies have highlighted the efficacy of fluoride adsorption with materials such as alumina, aluminum, iron oxide, and phosphate. This is particularly notable as iron oxide, known for its cost-effectiveness, and composites, including aluminum oxide, exhibit significant fluoride adsorption capacity [3,7,8]. To incorporate these diverse adsorbents, we opted to synthesize composite materials using magnesium phosphate cement. This involved introducing varying amounts of aluminum, alumina, or iron oxide to investigate their respective adsorption capacities.

Magnesium phosphate cement (MPC), a type of chemical cement, was discovered and developed in the late 19th century [11]. Classified within the domain of construction materials, magnesium phosphate cements (MPCs) are recognized as a specific category of inorganic cementitious materials belonging to the phosphate cement family [12]. These cementitious materials are formulated at ambient room temperature through a neutralization reaction. This process involves combining basic magnesia with an acidic solution containing phosphates, commonly ammonium dihydrogen phosphate (ADP), supplemented with a setting retarder, typically from the boron family [10,13]. The chemical reaction yields the formation of the crystalline phase identified as struvite. This complex reaction can be accurately described by the following chemical equation:

$$MgO + NH_4H_2PO_4 + 5H_2O \rightarrow MgNH_4PO_4 \cdot 6H_2O \text{ (struvite)} \tag{1}$$

The uniqueness of this cement stems from its outstanding features: minimal permeability, accelerated strength gain, high initial strength, adhesive properties, and minimal drying shrinkage; moreover, MPCs demonstrate superior adaptability to changes in environmental temperature, a swift hydration process, solid durability, and rapid setting [14,15]. The distinctive characteristics of magnesium phosphate cement (MPC) pave the way for a wide range of applications, extending across civil engineering and the solidification and stabilization of nuclear waste [6]. Furthermore, within the medical domain, this cement demonstrates its value by serving applications in biomedical materials and contributing to bone restoration [13,16,17]. Despite the interesting characteristics of this type of cement, it presents disadvantages. It is essential to delve deeper into these persistent drawbacks. Its limited water resistance poses a challenge, and solving this problem requires innovative solutions. Its short, difficult-to-regulate setting period can hinder flexibility in various

construction applications, requiring advanced techniques to extend working times without compromising performance. Additionally, reduced porosity, although characteristic of magnesium phosphate cement, requires research and development to improve its permeability for specific use cases. By addressing these aspects, progress can be made to alleviate the disadvantages and further optimize the performance of magnesium phosphate cement in practical applications [12]. In recent years, there has been a growing focus on the study of MPC-based repair materials. Research efforts primarily delve into the refinement of their preparation techniques, the exploration of modification mechanisms, and the assessment of their performance in conventional environmental settings.

The primary objective of this study is to enhance the resistance of magnesium phosphate cement when exposed to water by developing various composite materials. These composites will incorporate reinforcing elements such as aluminum, alumina, or iron oxide. Additionally, the study aims to investigate and optimize their capacity for adsorbing fluorine, a critical aspect of water treatment processes.

2. Material and Methods

2.1. Materials

In this study, cement pastes were meticulously prepared by blending weighted portions of powders, including high-purity magnesium oxide (MgO > 99%—Merck KGaA Frankfurter Str.25, Darmstadt, Germany), dihydrogen ammonium phosphate ($NH_4H_2PO_4$ > 99%—SIGMA-ALDRICH (Darmstadt, Germany)), borax, aluminum, alumina, and iron oxide. All raw materials were sourced from Sigma Aldrich (Darmstadt, Germany), ensuring consistency and quality. To reduce reactivity, magnesium oxide was calcined at 1500 °C for 6 h, resulting in dead-burned magnesia. Furthermore, in this research, we chose to exclude aggregates. The omission of aggregates is essential to preserving material purity during synthesis, as they have the potential to jeopardize the quality of the end product. The process entails regulating particle size, and the optimization of synthesis conditions involves fine-tuning parameters to minimize the likelihood of aggregates while maximizing yield [18].

2.2. Preparation

The synthetic protocol for creating the diverse composites starts with the mixing process, which involves carefully combining magnesium and acid in a precise ratio of Mg/P = 1, with the addition of distilled water. Following this, an optimal quantity of aluminum powder, aluminum oxide, or iron oxide is added, and rapid manual mixing ensues until a uniform paste is achieved. This step-by-step approach ensures a homogeneous distribution of components in the composites.

Various materials are formulated using a consistent cement matrix. The Al-cement is prepared by incorporating 1.5320 g of aluminum, while the sample S_1 includes 1.5640 g of aluminum and an additional 1.5320 g of Fe_2O_3. Moreover, the 0.25 g Al-cement is prepared using only 0.25 g of aluminum. The fourth synthesized material, named S_2, contains 0.2500 g of aluminum and 0.5470 g of alumina (Al_2O_3). These various synthesized materials are subsequently characterized for optimal quantities and utilized for the retention of fluorides.

Table 1 provides an overview of the chemical compositions of the various composites.

Table 1. Chemical compositions of synthesized samples.

	MgO (g)	$NH_4H_2PO_4$ (g)	Borax (g)	Al (g)	Al_2O_3 (g)	Fe_2O_3(g)	H_2O (mL)
Al-cement	1.0680	2.8580	0.3115	1.5320	-	-	2
S_1	1.0320	2.8628	0.3330	1.5640	-	1.5320	2
0.25 g Al-cement	1.0790	2.8800	0.3310	0.2560	-	-	2
S_2	1.0390	2.8580	0.3250	0.2500	0.5470	-	2

2.3. Analysis Method

The powder structure analysis was conducted using wide-angle X-ray diffraction. For every cement paste preparation, we used the X'per PRO PANalytical powder diffractometer (Philips, Farnborough, UK) with CuKα radiation (λKα = 1.54 Å) to identify the crystalline phases. Moreover, a comparative study of compounds synthesized using pure cement and Al-cement was provided.

Diffraction patterns were collected in the range of $10° < 2\theta < 80°$. The microstructures of the magnesium phosphate cement (MPC) pastes were examined using scanning electron microscopy (SEM) equipped with an energy dispersive spectrometer (EDS) (SEM, (JEOL)-Akishima, Japan) to analyze their elemental compositions. Thermal behavior was investigated through a thermogravimetric analysis (TGA, Perkin-Elmer, Waltham, MA, USA), tracking the mass evolution of samples subjected to temperature increments from 20 to 1150 °C at a heating rate of 20 °C/min^{-1}. Additionally, we determined the specific surface areas using the Brunauer–Emmett–Teller (BET) method (TriStar 3000 V6.06 A, Stevenage, UK) to examine the dehydration characteristics of struvite. Furthermore, the FTIR spectra were recorded in the 4000–400 cm^{-1} range using 32 scans at a nominal resolution of 4 cm^{-1} using a Perkin Elmer 100 FT spectrophotometer equipped (FTIR, Perkin-Elmer, USA) with an ATR Diamant unit and an MCT detector (liquid nitrogen).

2.4. Adsorption Study

The fluoride adsorption process was conducted at a consistent pH and room temperature (25 $\pm$ 2 °C) across all samples. The mass of solids used was standardized at 0.3 g for all materials. The solids were introduced into 20 mL tubes, each containing a fluoride solution with different initial concentrations ranging from 20 to 400 mg/L. The mixtures were stirred at 200 rev/min for a duration of one night (15 h). Subsequently, 0.2 µm filters were employed for filtration, and the filtrate was analyzed for its residual fluoride concentration using a fluorine-specific electrode.

The following equation (Equation (2)) was used to determine the amount of adsorbed fluoride [19], q_e (mg/g):

$$q_e = \frac{(C_0 - C_e) \times V}{m} \tag{2}$$

where m is the mass of the adsorbent (g), V is the volume of the solution (L), and C_0 and C_e are the initial and final concentrations of fluoride in the solution (mg/L).

Throughout the experiments, the pH is intentionally maintained constant within the range of 8 to 9. This choice is deliberate to minimize the potential influence of pH fluctuations on the adsorption process, thereby ensuring the reliability and consistency of our results.

3. Results and Discussion

3.1. Composites Analyses

The microstructures of the various synthesized cement pastes were examined and are presented in Figure 1. The SEM images are organized as follows: Figure 1(a1,a2) correspond to the material named S_1, Figure 1(b1,b2) relate to material S_2, and Figure 1(c1,c2) specifically represent Al-cement, a sample prepared with 1.5 g of aluminum. Additionally, the EDX analysis of materials S1 and S2 is presented in Figure 2.

As shown in Figure 1, the microstructures of the various materials exhibit a dense composition with tubular crystals predominantly in rod-like forms [6]. Additionally, a minor level of porosity is observed, primarily resulting from the significant gas evolution during the synthesis. Despite this, the structure demonstrates heightened strength, enhanced resistance to water contact, and remarkable stability. Notably, even after continuous stirring for several days, the solid structure remains intact.
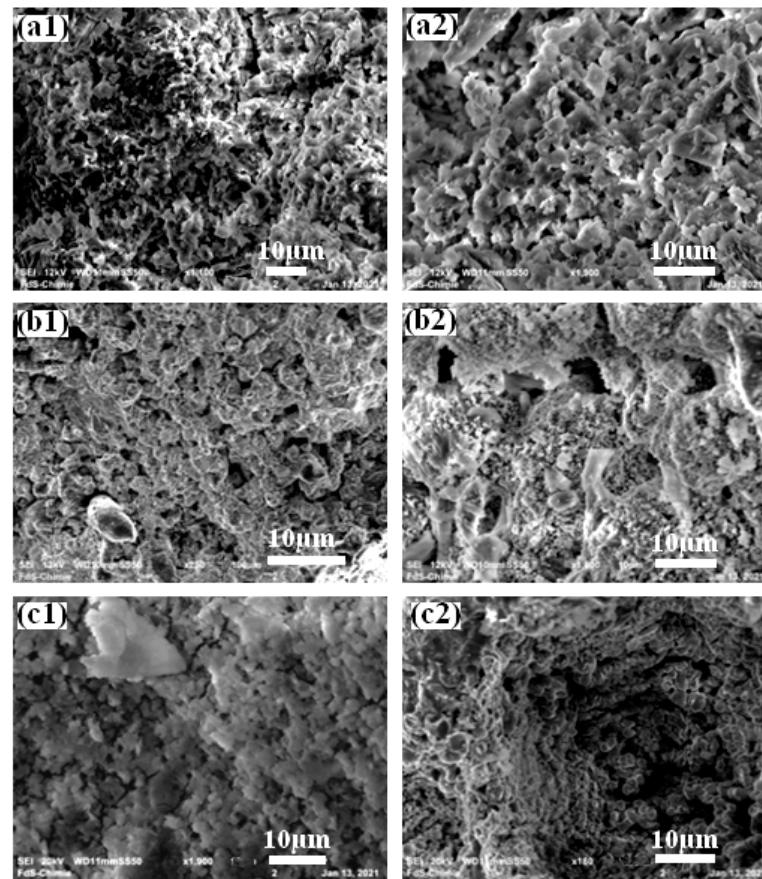
Figure 1. SEM of composites (**a1**,**a2**) S_1 and (**b1**,**b2**) S_2 and (**c1**,**c2**) Al-cement samples.
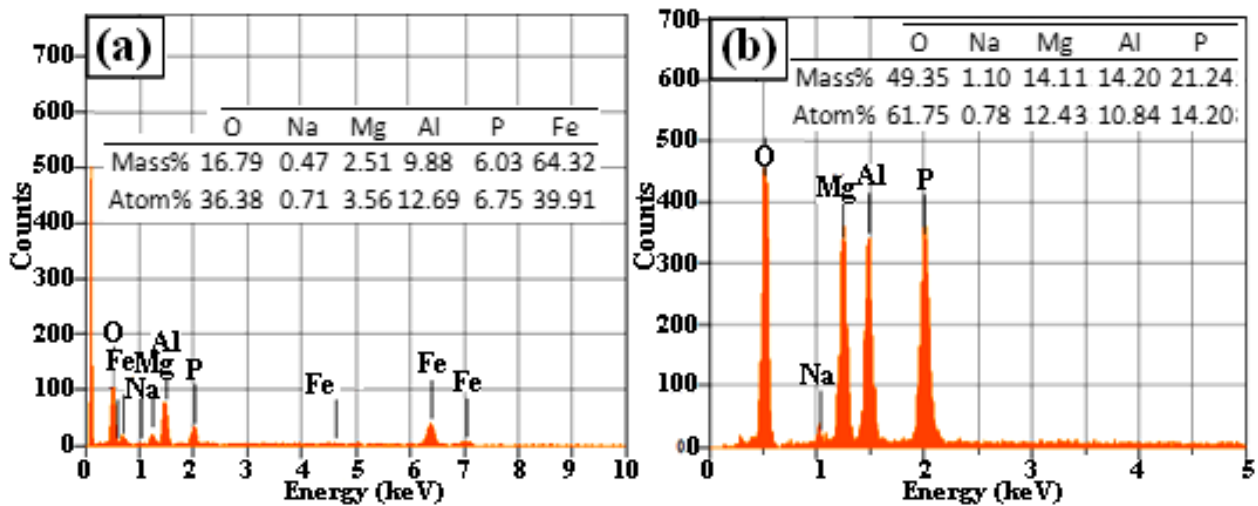

Figure 2. EDS analyses of (**a**) S_1 and (**b**) S_2 composites.

On the other hand, the incorporation of iron oxide yields a denser and more compact structure. The EDS analysis of this material validates the presence of trace amounts of phosphorus (P), sodium (Na), magnesium (Mg), and aluminum (Al) (Figure 2). This analysis confirms nearly complete acid dissolution and minimal unreacted MgO while underscoring the prominent presence of iron oxide. Moreover, the EDS analysis of the composite synthesized with an alumina addition confirms the presence of aluminum (Al), along with traces of magnesium (Mg), phosphorus (P), and sodium (Na).

The thermal gravimetric analysis (TGA) curves for the various composites are illustrated in Figure 3. Both synthesized materials display similar thermal behaviors, characterized by an initial weight loss starting at T = 50 °C and the process finishing near T = 700 °C. The total mass loss for S_1 is approximately 22.89%, whereas for S_2, it amounts to approximately 39.86%. This mass loss can be attributed to the decomposition of the material, occurring in two distinct stages [6,11].
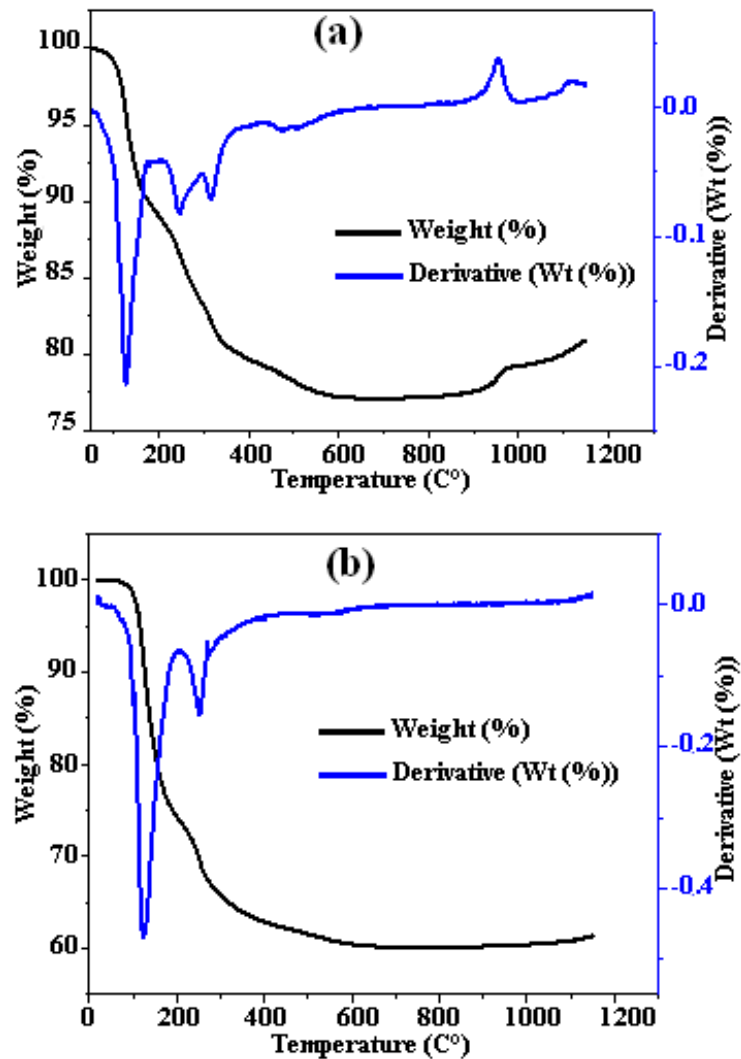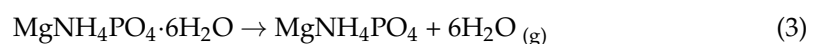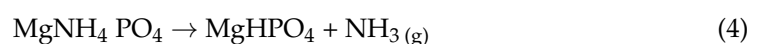

Figure 3. TGA curves of different composites (**a**) S_1 and (**b**) S_2.

The decomposition observed between 50 and 300 °C is attributed to dehydration [6,10], represented by the following reaction:

$$MgNH_4PO_4 \cdot 6H_2O \rightarrow MgNH_4PO_4 + 6H_2O_{(g)} \tag{3}$$

The decomposition reaction of the material occurs in the interval 300 to 700 °C, expressed in terms of:

$$MgNH_4\,PO_4 \rightarrow MgHPO_4 + NH_{3\,(g)} \tag{4}$$

For both composites synthesized with 1.5 g of aluminum, the specific surface of the aluminum-based cement is greater than that prepared by adding the same amount of iron oxide (Table 2). As shown, one can note that it is almost three times greater.

Table 2. Specific surface area, pore volume, and pore size values of different prepared samples.

	BET Surface	Pore Volume	Pore Size
1.5 g-Al-cement	64.0342 ± 3.7 m^2/g	0.060498 cm^3/g	37.7913 Å
S_1	21.8228 ± 1.2 m^2/g	0.030965 cm^3/g	56.7565 Å
0.25 g-Al-cement	83.524 ± 3.3 m^2/g	0.074313 cm^3/g	35.5886 Å
S_2	134.673 ± 2.3 m^2/g	0.15054 cm^3/g	44.715 Å

This increase is due to the strong release of gas during the synthesis of the cement. In contrast, the composites synthesized with only 0.25 g of aluminum or by adding 0.5 g of alumina exhibit a significantly greater surface area compared to the other two types of cement (Table 2). Additionally, the incorporation of alumina has a pronounced positive impact on the structural properties. According to Figure 4, it is evident that the specific surface area notably increases to approximately 134.6 m^2/g. For each of the synthesized materials, the hysteresis curve is type II, commonly observed in BET analyses, suggesting the appearance of multilayer adsorption and adsorption on low-porosity surfaces. These phenomena generally begin at higher pressures. The hysteresis loop is type H4, in particular, indicating that the sample includes divided pores with a size distribution mainly in the microporous range [6,11].
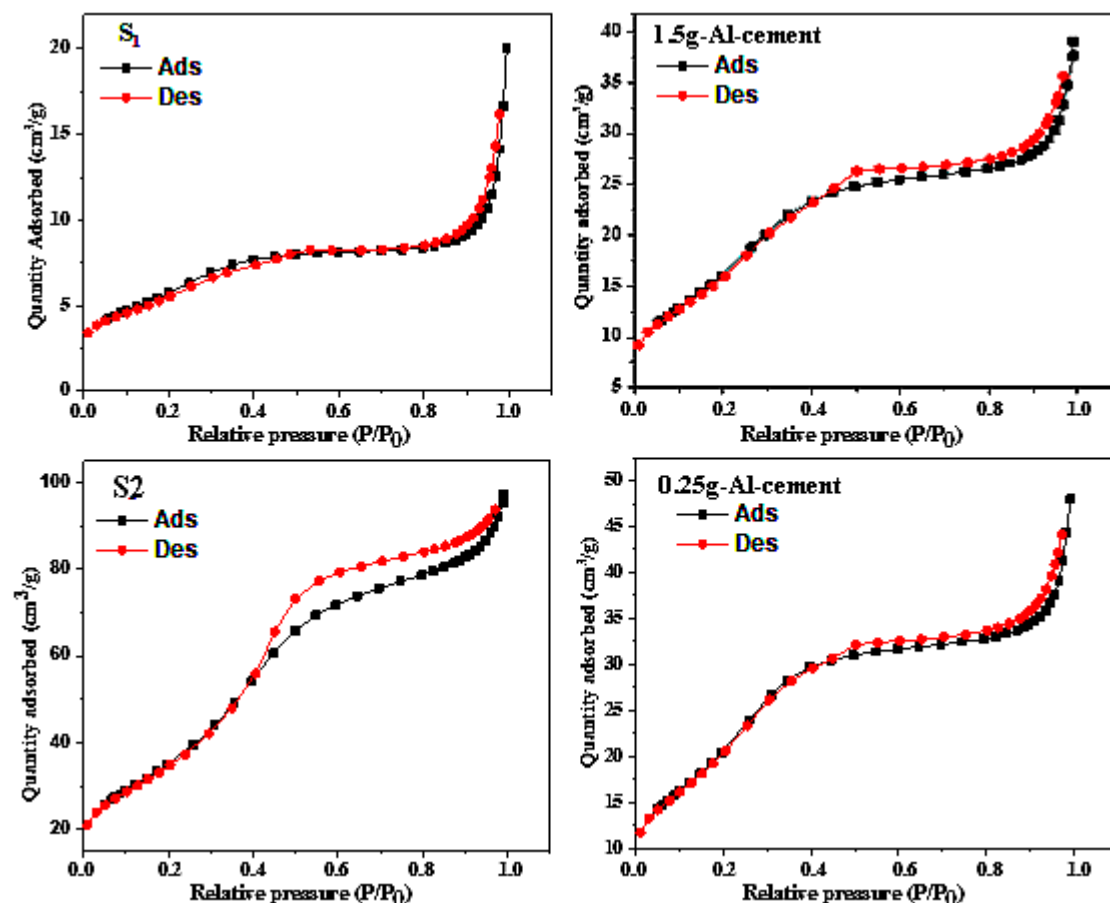
Figure 4. N$_2$ adsorption/desorption curves for different samples: 0.25-Al-cement, 1.5 g-Al-cement, S_1, and S_2.

An analysis of powder structure was conducted, and Figure 5 demonstrates a comparative study of the diffractograms of compounds synthesized using both pure cement and Al-cement.
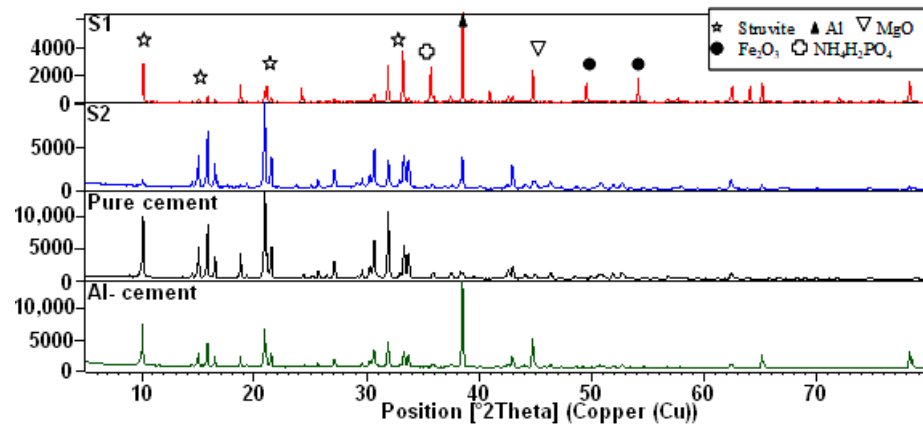
Figure 5. X-ray diffraction pattern of different composites: S_1, S_2, pure cement, and Al-cement.

The overlay of diffraction patterns confirms a distinct peak characteristic of struvite, which is the stable phase of cement, observed around 21°-2-theta. This peak signifies the crystallization of the material. Minor peaks attributed to unreacted magnesia were observed at approximately 43°, along with peaks indicating the presence of residual $NH_4H_2PO_4$ within the 30–33° 2-theta range. The main peaks associated with aluminum were identified in the 2θ range of 38–39°. Furthermore, iron oxide exhibited a prominent peak at an average of 50–54° 2-theta. It is noteworthy that no new phases were formed, indicating the material's ability to maintain its stable structure, attributed to the addition of aluminum, alumina, or iron oxide. Moreover, this enhanced composition resulted in improved cement hardness and water resistance [8,16].

Figure 6 presents the FTIR data for the composite cement. Both composites display similar bonding patterns, albeit with slight shifts towards shorter or longer wavelengths. The peak at 559 cm^{-1} is attributed to the bending modes of the P-O bonds in the phosphate groups. Distinctive Al-O stretching vibrations are observed in the range of 559 to 754 cm^{-1}, as well as at 1655 cm^{-1}, corresponding to the transient and stable phases of alumina (AlO_4 or AlO_6 vibrations). The adsorption bonds at 985 and 2346 cm^{-1} can be attributed to the asymmetry of P-O vibrations in PO_4^{3-} within the cement. The prominent peak at 2842 cm^{-1} is associated with the unsymmetrical stretching vibration of N–H in NH_4^+. Additionally, a smaller peak indicating the unsymmetrical bending vibration of the NH_4^+ group appears around 1432 cm^{-1}. Furthermore, the peak observed at approximately 3226 cm^{-1} confirms the presence of the –OH stretching bond in chemisorbed water [20–23]. For sample S1, a noticeable stretching vibration at 2940 and 2920 cm^{-1}, respectively, is specific to the CH2 and CH3 groups and is probably caused by the solvent used to clean the crystal. Also, the –OH stretching bond observed at 3560 cm^{-1} may be a further consequence of this cleaning solvent.
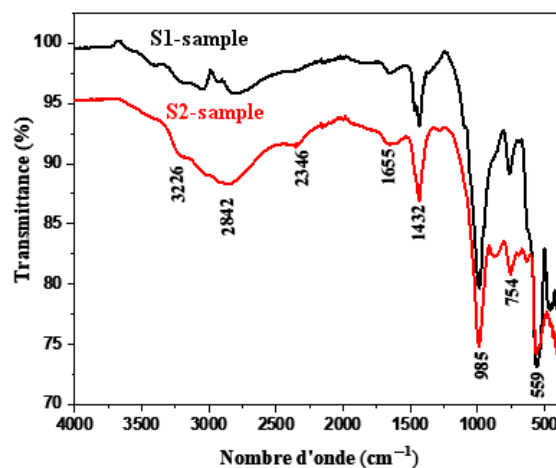

Figure 6. FTIR of different composites.

3.2. Adsorption Study

In order to assess the impact of various synthesized materials on fluoride removal efficiency, these solids were examined at varying concentrations. As depicted in Figure 7, it is evident that the rate of fluoride removal increased with higher initial concentrations.
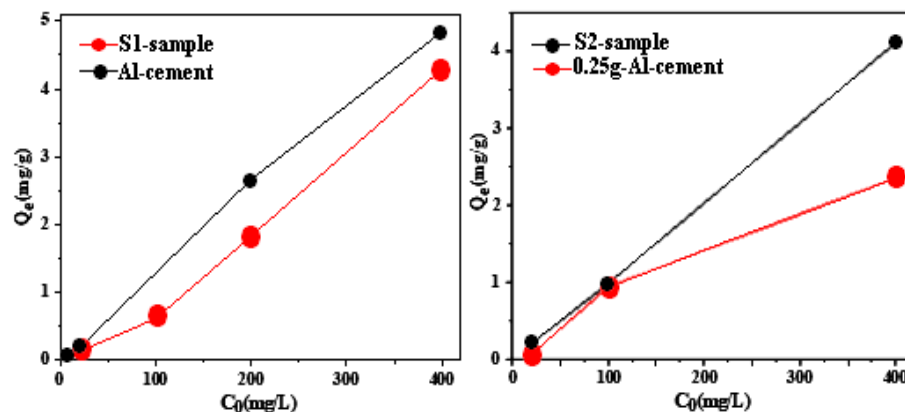

Figure 7. Influence of the initial concentration of fluoride on adsorption.

The adsorption capacity of various composite materials has been investigated and is presented in Figure 7. Notably, a comparison of the adsorption capacities between the two materials synthesized with 1.5 g of Al, one with and one without the addition of iron oxide, reveals that the Al-cement composite exhibits a higher adsorbed quantity compared to its iron oxide addition counterpart, measuring 4.84 mg/g and 4.29 mg/g, respectively. Furthermore, it is evident that the inclusion of alumina positively influences fluoride retention. For instance, the fluoride retention increases from 2.35 mg/g for the composite synthesized with 0.25 g of aluminum to 4.10 mg/g with the addition of only 0.5 g of alumina.

The adsorption isotherms illustrate the connection between the extent of adsorption and the concentration of the solute. By providing a detailed insight into the effectiveness of various materials, the isotherm enables the determination of the maximum quantity of adsorbed fluoride [22]. Equilibrium studies were conducted utilizing different isotherms. Various isotherms, such as the Langmuir, Freundlich, Temkin, and Dubinin–Radushkevich isotherms, are utilized to gain a comprehensive understanding of the adsorption process. The Langmuir isotherm effectively portrays monolayer adsorption, signifying that adsorbate molecules arrange themselves in a single layer on the adsorbent surface. This model assumes a uniform surface with a fixed number of identical adsorption sites, neglecting interactions between adsorbate molecules.

Conversely, the Freundlich isotherm characterizes multilayer adsorption, indicating that adsorbate molecules can form multiple layers on the surface. This model is suitable for heterogeneous surfaces with varying adsorption energies, providing flexibility in representing the adsorption process.

The Temkin isotherm takes into account the indirect interactions between the adsorbate and the adsorbent, introducing the concept of a uniform distribution of binding energies. It assumes a linear decrease in adsorption energy as the surface coverage increases.

Lastly, the Dubinin–Radushkevich isotherm is employed for microporous adsorbents and describes the adsorption process in terms of the volume filling of micropores.

By employing these diverse isotherms, we can unravel the complex dynamics of adsorption, capturing various aspects of the interaction between adsorbate molecules and the adsorbent surface [19,24]. Each isotherm is characterized by an equation that posits specific assumptions and identifies the prevailing adsorption mechanism, as presented in Table 3 [25,26]. Referring to Figure 8 and Table 3 and considering the correlation coefficient, R^2, it is evident that both materials adhere to Langmuir's isothermal model, indicating

monolayer adsorption. Furthermore, the determined R_L separation factor affirms the favorable nature of the adsorption.

Table 3. Values of different parameters of Langmuir, Freundlich, Temkin, and Dubinin–Radushkevich isotherms for both composites S_1 and S_2.

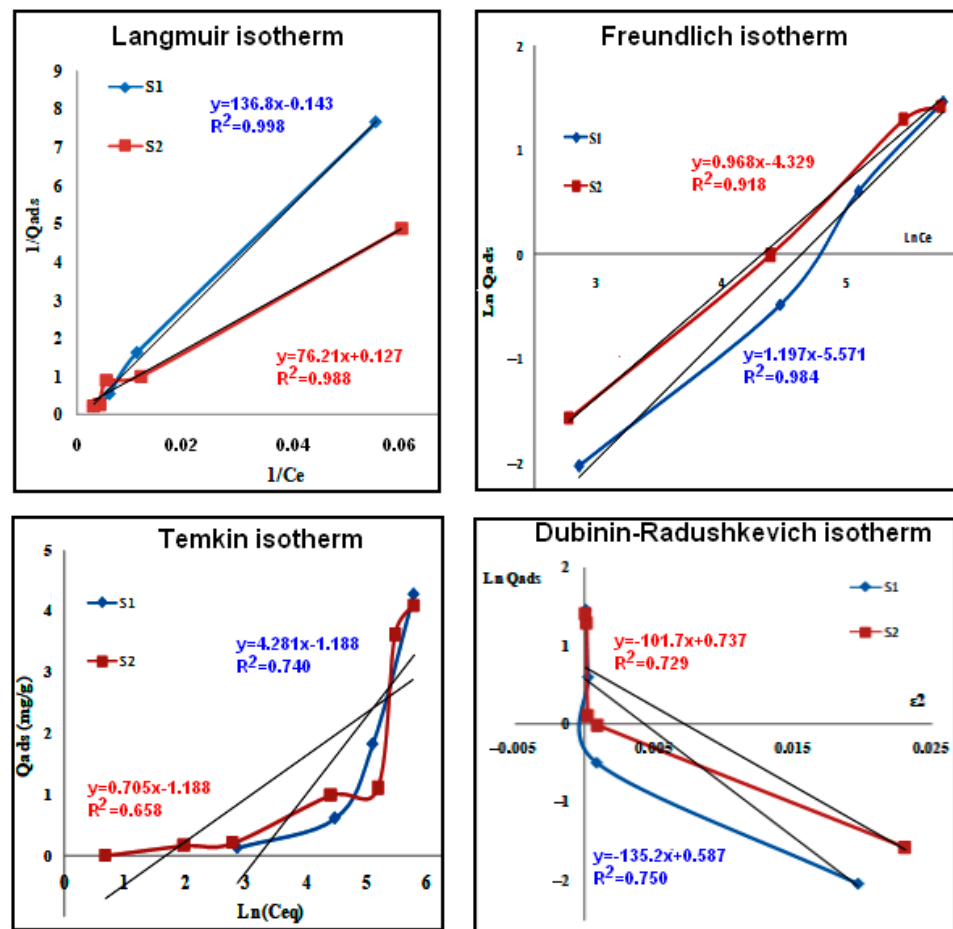| Isotherm	Equation	S_1	S_2
Langmuir	$\frac{1}{q_e} = \frac{1}{q_m} + \frac{1}{q_m b c_e}$	b = 0.205 L/g q_0 = 4.87 mg/g R_l = 0.806 K_{ap} = −0.0010 R^2 = 0.998	b = 0.023 L/g q_0 = 43.47 mg/g R_l = 0.993 K_{ap} = 0.0016 R^2 = 0.988
Freundlich	$\log q_e = \log K_f + \frac{1}{n} \log C_e$	1/n = 1.197 K_f = 0.0038 R^2 = 0.999	1/n = 0.968 K_f = 0.0131 R^2 = 0.918
Temkin	$q_e = \frac{RT}{b} \ln A + \frac{RT}{b} \ln C_e$	A = 0.040 B = 1.281 R^2 = 0.740	A = 0.185 B = 0.705 R^2 = 0.658
Dubinin–Radushkevich	$\ln q\,\varepsilon = \ln q_m - \beta\,\varepsilon^2$	q_d = 0.951 B = −135.2 R^2 = 0.750	q_d = 1.799 B = 101.7 R^2 = 0.729

Figure 8. Modeling of composites according to Langmuir, Freundlich, Temkin, and Dubinin–Radushkevich isotherms.

3.3. Comparison with Other Used Adsorbents

A comparison of the two synthesized materials with other composites studied in previous articles [5,9], as well as with various adsorbents, reveals significant information (Table 4). The introduction of iron oxide into the cement matrix alongside aluminum slightly reduced the adsorption amount from 4.48 mg/g to 4.29 mg/g. Conversely, the incorporation of alumina results in an improved adsorption capacity, increasing from 2.35 mg/g to 4.10 mg/g with a simple addition of 0.5 g of alumina. It should be noted that the inclusion of alumina has a favorable impact on the retention of fluoride within the aluminum-based cement matrix compared to peroxide. The adsorbed quantity increases from 1.61 mg/g to 4.10 mg/g with the addition of alumina.

Table 4. Comparison of removal capacity of the present composites with others previously studied.

Adsorbent	Removal Capacity (mg/g)	pH	Refs.
Portland Pozzolana Cement	0.25	6–11.8	[27]
Calcite	0.39	6	[28]
Mg-HAP	1.40	9–10	[29]
Alumina cement	1.61	8–10	[10]
0.25 g Al-cement	2.35	8–9	Present study
1.5 g Al-cement	4.84	8–9	Present study
Composite S_1 cement	4.29	8–9	Present study
Composite S_2 cement	4.10	8–9	Present study

4. Conclusions

A novel composite material based on magnesium phosphate cement was successfully synthesized by incorporating varying amounts of aluminum, alumina, or iron oxide. The primary objective was to enhance the properties of this cement in both water and dry environments, as well as assess its capability to adsorb fluoride. The analyses conducted led to several significant conclusions:

- The addition of iron oxide, aluminum, and alumina significantly enhances the strength of the cement matrix, improving its resistance to water and dry conditions even after several days of direct contact. Notably, the addition of alumina has the additional benefit of reducing the exothermicity of the reaction, improving the cement's setting time.
- The addition of aluminum or alumina to the cement matrix enables an improvement in the specific surface area of the material.
- The highest adsorption capacity for fluoride observed was 4.84 mg/g, achieved with the material synthesized using 1.5 g of aluminum.
- Incorporating iron oxide into a matrix containing 1.5 g of aluminum slightly decreases the adsorbed quantity, shifting from 4.84 mg/g to 4.29 mg/g.
- An alumina addition markedly improves adsorption, especially for the composite initially containing only 0.25 g of aluminum, increasing from 2.35 mg/g to 4.10 mg/g with the addition of a mere 0.5 g of alumina.
- The Langmuir isotherm aptly describes the adsorption process, indicating monolayer adsorption, where adsorbate molecules form a single layer on the adsorbent surface. This model assumes a homogeneous surface with a fixed number of identical adsorption sites and does not account for interactions between adsorbate molecules. Additionally, the calculated separation factor, R_L, further confirms the favorable nature of the adsorption process.

The modification of magnesium phosphate cement with aluminum, iron oxide, or alumina demonstrates promising potential as an effective adsorbent for fluoride removal, showcasing remarkable fluoride adsorption capabilities.

Author Contributions: Conceptualization, A.H.A., C.C. and M.C.; Formal analysis, S.G. and M.C.; Investigation, A.A.; Resources, A.A.; Data curation, M.C.; Writing—original draft, S.G.; Writing—review & editing, A.A., A.H.A. and C.C.; Supervision, M.C. All authors have read and agreed to the published version of the manuscript.

Institutional Review Board Statement: Not applicable.

Informed Consent Statement: Not applicable.

Data Availability Statement: Data can be requested from the authors.

Conflicts of Interest: The authors declare no conflict of interest.

References

1. Schweitzer, L.; Noblet, J. Chapter 3.6—Water Contamination and Pollution. *Green Chem.* **2018**, 261–290. [CrossRef]
2. Ben Mbarek, W.; Pineda, E.; Escoda, L.; Suñol, J.J.; Khitouni, M. High-efficiency decolorization of azo dye Reactive Black 5 by Ca-Al particles. *J. Environ. Chem. Eng.* **2017**, *5*, 6107–6113. [CrossRef]
3. Hafshejani, L.D.; Tangsir, S.E.; Daneshvar, M.; Maljanen, A.; Lähde, J.; Jokiniemi, M.; Naushad, M.; Bhatnagar, A. Optimization of fluoride removal from aqueous solution by Al_2O_3 nanoparticles. *J. Mol. Liq.* **2017**, *238*, 254–262. [CrossRef]
4. Borgohain, X.; Boruah, A.; Sarma, G.K.; Rashid, M.H. Rapid and extremely high adsorption performance of porous MgO nanostructures for fluoride removal from water. *J. Mol. Liq.* **2020**, *305*, 112799. [CrossRef]
5. Karkar, S.; Debnath, S.; De, P.; Parashar, K.; Pillay, K.; Sashikumar, P.; Ghosh, U.C. Preparation, characterization and evaluation of fluoride adsorption efficiency from water of iron-aluminium oxide-graphene oxide composite material. *Chem. Eng. J.* **2016**, *306*, 269–279. [CrossRef]
6. Gharsallah, S.; Alsawi, A.; Hammami, B.; Khitouni, M.; Charnay, C.; Chemingui, M. Synthesis and Characterization of New Composite Materials Based on Magnesium Phosphate Cement for Fluoride Retention. *Materials* **2023**, *16*, 718. [CrossRef] [PubMed]
7. Mondal, P.; Purkait, M.K. Preparation and characterization of novel green synthesized iron aluminum nanocomposite and studying its efficiency in fluoride removal. *Chemosphere* **2019**, *235*, 391–402. [CrossRef] [PubMed]
8. Gasparotto, J.M.; Roth, D.; Perilli, D.O.; Franco, D.S.P.; Carissimi, E.; Foletto, E.L.; Jahn, S.L.; Dotto, G.L. A novel Fe-Al-La trioxide composite: Synthesis, characterization, and application for fluoride ions removal from the water supply. *J. Environ. Chem. Eng.* **2021**, *9*, 106350. [CrossRef]
9. Liu, X.; Xiao, M.; Li, Y.; Chen, Z.; Yang, H.; Wang, X. Advanced porous materials and emerging technologies for radionuclides removal from Fukushima radioactive water. *Eco-Environ. Health* **2023**, *2*, 252–256. [CrossRef]
10. Li, Y.; Zhang, G.; Hou, D.; Wang, Z. Fluoride adsorption properties of three modified forms of activated alumina in drinking water. *J. Water Health* **2014**, *12*, 715–721. [CrossRef]
11. Gharsallah, S.; Mallah, A.; Alsawi, A.; Hammami, B.; Khitouni, M.; Charnay, C.; Chemingui, M. Study of Modified Magnesium Phosphate Cement for Fluoride Removal. *Materials* **2023**, *16*, 5749. [CrossRef]
12. Li, Y.; Zhang, G.; Hou, D.; Wang, Z. Nanoscale insight on the initial hydration mechanism of magnesium phosphate cement. *Constr. Build. Mater.* **2021**, *276*, 122213. [CrossRef]
13. Ribeiro, D.V.; Morelli, M.R. Influence of the addition of grinding dust to a magnesium phosphate cement matrix. *Constr. Build. Mater.* **2009**, *23*, 3094–3102. [CrossRef]
14. Le Rouzic, M.; Chaussadent, T.; Stefan, L.; Saillio, M. On the influence of Mg/P ratio on the properties and durability of magnesium potassium phosphate cement pastes. *Cem. Concr. Res.* **2017**, *96*, 27–41. [CrossRef]
15. Tansel, B.; Lunn, G.; Monje, O. Struvite formation and decomposition characteristics for ammonia and phosphorus recovery: A review of magnesium-ammonia-phosphate interactions. *Chemosphere* **2018**, *194*, 504–514. [CrossRef]
16. Zhang, Q.; Cao, X.; Ma, R.; Sun, S.; Fang, L.; Lin, J.; Luo, J. Solid waste-based magnesium phosphate cements: Preparation, performance and solidification/stabilization mechanism. *Constr. Build. Mater.* **2021**, *297*, 123761. [CrossRef]
17. Lu, X.; Chen, B. Experimental study of magnesium phosphate cements modified by metakaolin. *Constr. Build. Mater.* **2016**, *123*, 719–726. [CrossRef]
18. Bouaoun, I.; Hammi, H.; M'nif, A. Box-Behnken design optimization of magnesium potassium phosphate cement properties using sodium chloride as retarder. *J. Tunis. Chem. Soc.* **2016**, *18*, 152–159.

19. Limousin, G.; Gaudet, J.P.; Charlet, L.; Szenknect, S.; Barthès, V.; Krimissa, M. Sorption isotherms: A review on physical bases, modeling and measurement. *Appl. Geochem.* **2007**, *22*, 249–275. [CrossRef]
20. Ding, Z.; Dong, B.; Xing, F.; Han, N.; Li, Z. Cementing mechanism of potassium phosphate based magnesium phosphate cement. *Ceram. Int.* **2012**, *38*, 6281–6288. [CrossRef]
21. Sotiriadis, K.; Mácová, P.; Mazur, A.S.; Tolstoy, P.M.; Viani, A. A solid state NMR and in-situ infrared spectroscopy study on the setting reaction of magnesium sodium phosphate cement. *J. Non-Cryst. Solids* **2018**, *498*, 49–59. [CrossRef]
22. Spirovski, F.; Kuzmanovski, I.; Lutz, H.D.; Engelen, B. Infrared and Raman spectra of magnesium ammonium phosphate hexahydrate (struvite) and its isomorphous analogs. I. Spectra of protiated and partially deuterated magnesium potassium phosphate hexahydrate. *Mol. Struct.* **2004**, *689*, 110. [CrossRef]
23. Chu, Y.; Khan, M.A.; Zhu, S.; Xia, M.; Lei, W.; Wang, F.; Xu, Y. Microstructural modification of organo-montmorillonite with Gemini surfactant containing four ammonium cations: Molecular dynamics (MD) simulations and adsorption capacity for copper ions. *J. Chem. Technol. Biotechnol.* **2019**, *94*, 3585–3594. [CrossRef]
24. Foo, K.Y.; Hameed, B.H. Insights into the modeling of adsorption isotherm systems. *Chem. Eng. J.* **2010**, *156*, 2–10. [CrossRef]
25. Zhu, S.; Khan, M.A.; Wang, F.; Bano, Z.; Xia, M. Exploration of adsorption mechanism of 2-phosphonobutane-1,2,4-tricarboxylic acid onto kaolinite and montmorillonite via batch experiment and theoretical studies. *J. Hazard. Mater.* **2021**, *403*, 123810. [CrossRef] [PubMed]
26. Chaudhary, M.; Jain, N.; Maiti, A. A comparative adsorption kinetic modeling of fluoride adsorption by nanoparticles and its polymeric nanocomposite. *J. Environ. Chem. Eng.* **2021**, *9*, 105595. [CrossRef]
27. Shyamal, D.S.; Ghosh, P.K. Efficiency of Portland Pozzolana Cement as an adsorbent in removing excess fluoride from groundwater. *Groundw. Sustain. Dev.* **2019**, *9*, 100248. [CrossRef]
28. Fan, X.; Parker, D.J.; Smith, M.D. Adsorption kinetics of fluoride on low-cost materials. *Water Res.* **2003**, *37*, 4929–4937. [CrossRef]
29. Mondal, P.; George, S. Removal of Fluoride from Drinking Water Using Novel Adsorbent Magnesia-Hydroxyapatite. *Water. Air. Soil Pollut.* **2015**, *226*, 241. [CrossRef]